Article:

Sun, Q, Jackson, CAL, Magee, C orcid.org/0000-0001-9836-2365 et al. (1 more author) (2020) Deeply buried ancient volcanoes control hydrocarbon migration in the South China Sea. Basin Research, 32 (1). pp. 146-162. ISSN 0950-091X

https://doi.org/10.1111/bre.12372

Deeply buried ancient volcanoes control hydrocarbon migration in the South China Sea

Qiliang Sun[1,2,3*], Christopher A.L. Jackson[4], Craig Magee[5], and Xinong Xie[1,3]

[1]Key Laboratory of Tectonics and Petroleum Resources, China University of Geosciences (Wuhan), Ministry of Education, Wuhan 430074, China;

[2]Laboratory for Marine Mineral Resources, Qingdao National Laboratory for Marine Science and Technology, Qingdao 266061, China;

[3]College of Marine Science and Technology, China University of Geosciences (Wuhan), Wuhan, Hubei 430074, PR China;

[4]Basins Research Group (BRG), Department of Earth Science & Engineering, Imperial College, London, SW7 2BP, UK;

[5]School of Earth and Environment, University of Leeds, Leeds, LS2 9JT, UK

Abstract

Seismic reflection data image now-buried and inactive volcanoes, both onshore and along the submarine portions of continental margins. However, the impact that these volcanoes have on later, post-eruption fluid flow events (e.g. hydrocarbon migration and accumulation) is poorly understood. Determining how buried volcanoes and their underlying plumbing systems influence subsurface

*Corresponding author: Dr. Qiliang Sun
Telephone/fax: +86 27 67886167
E-mail address: sunqiliang@cug.edu.cn.

fluid or gas flow, or form traps for hydrocarbon accumulations, is critical to de-risk hydrocarbon exploration and production. Here we focus on evaluating how buried volcanoes affect the bulk permeability of hydrocarbon seals, and channel and focus hydrocarbons. We use high-resolution 3D seismic reflection and borehole data from the northern South China Sea (SCS) to show how ~<10 km wide, ~<590 m high Miocene volcanoes, buried several kilometers (~1.9 km) below the seabed and fed by a sub-volcanic plumbing system that exploited rift-related faults: (i) acted as long-lived migration pathways, and perhaps reservoirs, for hydrocarbons generated from even more deeply buried (~8-10 km) source rocks; and (ii) instigated differential compaction and doming of the overburden during subsequent burial, producing extensional faults that breached regional seal rocks. Considering that volcanism and related deformation are both common on many magma-rich passive margins, the interplay between the magmatic products and hydrocarbon migration documented here may be more common than currently thought. Our results demonstrate that now-buried and inactive volcanoes can locally degrade hydrocarbon reservoir seals and control the migration of hydrocarbon-rich fluids and gas. These fluids and gases can migrate into and be stored in shallower reservoirs, where they may then represent geohazards to drilling and impact slope stability.

Keywords

Hydrocarbon, volcano, fault, seal, migration, South China Sea

Introduction

Extrusive and intrusive igneous rocks are widespread in sedimentary basins (e.g. Berndt et al., 2000; White et al., 2003; Jackson et al., 2013; Magee et al., 2016; Schofield et al., 2017; Weinstein et al., 2017). Fluids and gases released in response to magmatism, such as hydrocarbons generated by intrusion-induced heating of source rocks or hydrothermal fluids derived from the magma itself, can migrate to shallower levels within basins and may even be expelled into the ocean or atmosphere (e.g. Lee et al., 2016; Hasenclever et al., 2017; Moussallam et al., 2017). For example, the synchronous and widespread extrusion of substantial volumes of methane-rich hydrothermal fluids, emanating from the tips of intruding igneous sills, may have triggered or contributed to ancient climate change events (e.g. Jamtveit et al., 2004; Svensen et al., 2004, 2012; Iyer et al., 2017; Reynolds et al., 2017). Aside from inducing formation of syn-emplacement fluid-escape structures (e.g. hydrothermal vents and volcanoes), fractured igneous intrusions can also provide fluid migration pathways long after their solidification (Rateau et al., 2013; Schofield et al., 2017). Networks of igneous intrusions may thus potentially divert fluids (e.g. hydrocarbons) into and reactivate ancient, now-buried extrusive vents and volcanoes, allowing fluids to migrate upwards and bypass significant thicknesses of strata (Holford et al. 2017). Several studies document how extrusive and intrusive components of igneous systems can inhibit fluid flow and create traps (e.g. Schutter, 2003; Monreal et al., 2009; Gudmundsson and Løtveit, 2014; Infante-Paez and Marfurt, 2017). Understanding how igneous systems impact later fluid flow events is critical to de-risking the exploration and production of hydrocarbon, water, and geothermal resources (e.g. Wohletz and Heiken, 1986; Babiker and Gudmundsson, 2004; Holford et al., 2017; Schofield et al., 2017).

Deciphering how igneous systems influence fluid flow events is problematic, because the physical properties (e.g. porosity and permeability) of intrusive and extrusive rocks can be highly heterogeneous over a range of scales (Millett et al., 2016), and related bodies can either act as reservoirs (e.g. Yang et al., 2016) or seals (e.g. Holford et al., 2012). Moreover, differential compaction of sedimentary rocks across (nearly) incompressible igneous rocks can cause folding and faulting (e.g. Zhao et al., 2014; Holford et al., 2017), which may facilitate or inhibit, post-magmatic fluid flow (Holford et al., 2017). Despite its clear importance, there are very few studies describing the precise control volcanoes and related overburden deformation have on post-magmatic fluid flow (e.g. Holford et al., 2017).

Here we use high-resolution 3D seismic data and borehole data to analyze spatial and temporal relationships between buried, Early Miocene volcanoes, pre- and post-eruption normal faults, and post-eruption free gas accumulations in the northern SCS. We show the presence of volcanoes instigated post-eruption, syn-burial overburden deformation, specifically differential compaction and normal faulting. These faults locally disrupted regional seals and allowed gas to ascend through the volcanic system into shallower reservoirs. Our results support recent findings that volcanoes and their underlying plumbing system can focus fluid (and gas) flow within sedimentary basins long after igneous activity has ceased (Holford et al., 2017).

Geological setting

The SCS is the largest (>3,500,000 km^2) and deepest (>5,000 m of water depth) marginal sea in the western Pacific Ocean. Seafloor spreading initiated in the northeast SCS in the Early Oligocene (~ 32.0 Ma) in response to the extensional Nanhai Event (e.g. Franke, 2013), before propagating to the southwest and ceasing at 15.0-15.5 Ma (Briais et al., 1993; Li et al., 2014). Post-spreading magmatism in the SCS has obscured seafloor spreading fabrics, making it difficult to precisely identify the timing of cessation of seafloor spreading (Sibuet et al., 2016).

The Pearl River Mouth Basin is one of several Cenozoic rift basins located on the northern continental margin of the SCS, covering an area of ~17.5×10^4 km^2, and comprising several NE-trending grabens, half grabens, and flanking massifs (Fig. 1a). During continental rifting (Late Cretaceous - Early Oligocene), non-marine mudstones and coals, which now represent the main hydrocarbon source rocks within the region, were deposited in the fault-bound depocentre sags (Zhang & Huang, 1991; Huang et al., 2003). During the syn-to-post rift transition (Late Oligocene - Early Miocene), marginal marine sandstones were deposited; these form the most important hydrocarbon reservoir units and carrier beds in the Pearl River Mouth Basin (Zhu et al., 2009). During the syn-to-post rift transition, the Nanhai Event caused three active periods of normal faulting (32-29 Ma, 23.8-21.0 Ma, and 18.5-16.5 Ma), which can be tied to initial opening, ridge jump, and maximum extension events in the SCS ocean basin (Deng et al., 2018). Deposition during the subsequent period of post-rift thermal subsidence (Early Miocene - Present), was dominated by very fine-grained, pelagic and hemipelagic strata, which provide an excellent regional seal (Zhu et al., 2009). Hydrocarbons were generated in the source rocks during the Early-Middle Miocene (Zhu et al., 2009). The latest Dongsha Event occurred from 10.5 Ma onwards, generating extensional faults that deform relatively young strata (Lüdmann & Wong, 1999; Zhao et al., 2012). These faults, together with highly permeable unconformities and mud diapirs, provided the main pathways for hydrocarbon migration in the northern SCS (Zhu et al., 2012).

The SCS lacks seaward-dipping reflectors (SDRs) and can thus be classified as magma-poor rifted margin (Yan et al., 2006; Franke, 2013). However, post-rift (Paleocene - Pliocene) magmatism, in the form of sills and relatively small, mafic-intermediate volcano complexes, are documented across the SCS (e.g. Zou et al., 1995; Yan et al., 2006; Franke, 2013; Li et al., 2014; Lester et al., 2014; Sun et al., 2014b; Zhao et al., 2014, 2016, 2018; Ma et al., 2018; Deng et al., 2018). The emplacement of subaerial and submarine volcanoes in the Pearl River Mouth Basin occurred during two main phases, during the Paleocene (57.1±2.5 Ma) and Early Miocene (17.1±2.5 Ma) (e.g. Li and Liang, 1994; Yan et al., 2006; Sun et al., 2014; Zhao et al., 2016; Deng et al., 2018). Early Miocene volcanoes were emplaced at broadly the same time as hydrocarbons *generation* in the deeply buried source rocks, but before the main stage of hydrocarbon *migration* (since ~10.5 Ma) (Zhu et al., 2012). Given their spatial and temporal relationship, and normal faults caused by the Nanhai Event may provide pathways for the Early Miocene volcanoes have been genetically related (Deng et al., 2018).

Data and Methods

We use a high-resolution 3D seismic dataset covering an area of ~530 km^2, in water depths of ~500-1200 m, and acquired in 2010 by a 3000 m long streamer with 240 channels. The dataset has a bin spacing of 12.5 m for both N-S oriented inlines and E-W oriented crosslines. The data is zero-phase processed and displayed with SEG (Society of Exploration Geophysicists) normal polarity, whereby a downward increase in acoustic impedance corresponds to a positive reflection (red on displayed seismic profiles). We use borehole data (well loggings, core cuttings, micropaleontology) from BY7-1 to constrain the lithology and age of the volcano-bearing succession and, thus, the age of volcano emplacement (Qin, 2000; Zhao et al., 2016; Ma et al., 2018) (Fig. 2). These borehole data also allow us to derive interval velocities for the volcanic complexes (~4500 m/s) and surrounding strata (~2800 m/s). Coupled with the dominant frequency of the seismic data, which gradually decreases downwards from the seabed (~45 Hz) to ~35 Hz where the volcano complexes are located, we estimate approximate limits of separability (λ/4) of ~32 m and ~20 m for the volcanic complexes and surrounding sedimentary strata, respectively (Zhao et al., 2016). Accordingly, we estimate the limit of visibility (λ/30) of the seismic data to be ~5 m for the volcanoes and ~3 m for sedimentary strata. For shallow strata at depths <500 m where no borehole data is available, an estimated velocity of 1700 m/s and a dominant frequency of ~45 Hz suggests limits of separability and visibility are ~10 m and ~5 m, respectively.

We mapped six regional stratigraphic boundaries, which we correlated to borehole BY7-1 (T0 (2.58 Ma), T1 (5.0 Ma), T2 (10.5 Ma), T4 (16.5 Ma), T5 (17.5 Ma) and T6 (23.8 Ma); e.g. Pang et al., 2007; Zhao et al., 2016; Deng et al., 2018; Ma et al., 2018) (Figs. 1b-c). We identify 14 mounded structures in the 3D seismic survey and map their top (TV) and base (BV); the former coincides with T5 (i.e. Early Miocene; Figs. 2-4). To identify and map free gas and normal faults, we extracted RMS attribute and variance slices from the 3D seismic volume (Fig. 5); the former measures the reflectivity of a given thickness (window) of seismic data and is calculated by dividing the square root of the sum of squared amplitudes with the number of samples within a specified window (Brown, 2004; Chopra and Marfurt, 2005) (Figs. 5f, 6). The variance, which is operated within a time window/interval, converts a volume of continuity (the normal reflections) into a volume of discontinuity and is free of interpretive bias (Brown, 2004; Chopra and Marfurt, 2005) (Figs. 5c-e).

Results

Buried volcanoes complexes

Composition and age

One of the 14 mounds we study here was drilled in 1988 by exploration borehole BY7-1 (Qin, 2000) (Figs. 2, 5a). The well shows that the mounded structure comprises mainly basalt and tuff, interbedded with a thin limestone layer and a thin claystone layer (Qin, 2000; Zhao et al., 2016; Ma et al., 2018) (Fig. 2). Based on its geometry and composition we therefore interpret the mounded structure as a volcano. The volcano intersected by BY7-1 is ~17.1±2.5 Ma (Early Miocene) based on K-Ar dating of a sample taken close to its top (Qin, 2000) (Fig. 2). Dead oil, i.e. residual oil without volatile components, occurs within samples from the volcano, as well as within the interbedded limestone (Fig. 2). Sub-volcanic strata are mainly composed of sandstone interbedded with volcanic material (basalt and tuff) and claystone. The oldest volcanic material intersected by BY7-1 yields a K-Ar date of 35.5±2.78 Ma (Middle Eocene) (Qin, 2000) (Fig. 2). Strata above the volcano comprise a ~260 m thick, Early Miocene sandstone package, which is overlain by Middle Miocene (and younger) claystone interbedded with several thin layers of sandstone and siltstone (Fig. 2). Well BY7-1 intersected free gas in the Early Miocene sandstone package and four younger, thinner, sandstone and siltstone layers (Fig. 2).

Seismic expression

The tops of the volcanoes are characterized by undulating, positive, high-amplitude seismic reflections (T5) (Fig. 4). Some volcanoes have relatively flat tops (<1°) whilst others are conical (Fig. 4). Volcano bases are relatively flat (Figs. 4a-b, 4d) and are characterized by a continuous, high-amplitude seismic event broadly conformable with underlying reflections (Fig. 4). Individual volcanoes are circular or elliptical, with their long axis trending WNW (~301°) (Figs. 3, 5a-b). Several volcanoes are connected to form linear complexes that trend WNW (~301°) (Figs. 3, 5a-b).

From their mapped external morphology, we calculate that volcano diameter and height ranges from 1–6 km and 50–590 m, respectively. Volcano flank dip ranges from ~1º to ~14º, and is typically >10º. The volcanoes cover a total area of at least ~245 km^2 and individually have a volume of at least ~62.5 km^3 (Fig. 5b).

The cores of individual volcanoes are usually characterized by chaotic seismic reflections, and layered seismic reflections; the latter may downlap the basal surface (T5; Fig. 4).

The volcanoes are onlapped and draped by post-eruption sedimentary strata of the Early Miocene Zhujiang Formation (Figs. 1b, 4). Strata directly overlying the volcanoes are typically folded and faulting, with dome-shaped folds being ~1–3 km wide and having amplitudes of ~350–1100 m (Figs. 4a, 7). The dome-shaped folds have similar sizes with the underlying volcanoes (Fig. 7). In some cases, seismic imaging is relatively poor directly above the volcanoes (including the dome-shaped folds) due to velocity wipe-out zones that are associated with anomalously low seismic frequencies (Figs. 4a, 7). The strata directly beneath the volcanoes are characterized by weak and chaotic seismic reflections (Figs. 4a-b) that are typically cut by normal faults (Figs. 1c, 8).

Seismic and geometrical characteristics of normal faults

Normal faults are widely developed across the study area. We distinguish two fault populations based on their distribution relative to the volcanoes: i.e. those largely restricted to sub-volcanic strata and those largely restricted to supra-volcanic strata.

Sub-volcanic faults

Normal faults within sub-volcanic strata (i.e. below surface T5) typically strike WNW-ESE (300±15º) (Figs. 7b, 8c-d, 5e, 9a), similar to the elongation trend of overlying volcanoes (Figs. 3, 5b, 9b-c). These faults are, on average, ~1.4 km long, but may reach lengths up to ~7.2 km (Figs. 9d, 9g). The faults are ~0.35–3.5 km tall (~85% are <1.1 km) and have throws of <160 m (Fig. 8c-d). Some of the largest normal faults (i.e. >3.0 km tall) in the pre-volcanic strata terminate directly beneath volcanoes (Figs. 7b, 8c-d), extending downwards into crystalline basement.

A few WNW-striking normal faults penetrate supra-volcanic strata shallower than T0 (~2.58 Ma), crossing-cutting the level at which the volcanic complexes are developed (Fig. 4c). These faults are >4.0 km tall (Fig. 4c), yet they are still relatively short in terms of their strike length (<6.1 km long) (Figs. 9e-f). These tall faults usually offset volcanoes that are associated with growth strata (i.e. volcano strata are thicker in the fault hangingwall than the footwall; Figs. 4c, 8a-b).

Supra-volcanic faults

Most supra-volcanic normal faults, especially those developed between T4 (16.5 Ma) and T1 (5.0 Ma), have limited vertical extents, ranging from ~0.3–2.0 km tall (Figs. 4a, 4c-d). Most (~68%) faults are <1.2 km tall. Supra-volcanic faults are usually rather short (typically < 3.0 km) in terms of their strike length (e.g. Fig. 9e and Fig. 9f), and the longest one reaches up to ~6.1 km long (Figs. 9e-f, h-i). The maximum displacement observed on the supra-volcano faults is ~90 m (Fig. 7). However, in some cases fault displacement cannot be quantified, especially where faults are poorly imaged below areas of free gas (see section below). The most important observations for the supra-volcanic faults is that they best-developed and most closely spaced (~0.4-2.0 km) directly above the volcanic complexes (Figs. 4, 5c-d), some terminating immediately above the underlying volcanoes

(Fig. 4a). The gross strike of these faults (WNW-ESE; ~300±15º) (Figs. 9b-c) is similar to the trends of the underlying volcanic complexes (Fig. 3).

Seismic expression and geochemical characteristics of free gas

Reflection anomalies characterized by anomalously low frequencies and negative polarity are frequently observed in the seismic profiles (Fig. 4). These anomalies are always located directly above the volcanoes (Figs. 6c-f), within the Middle Miocene and younger (i.e. supra-surface T5 strata; Figs. 4, 7). These anomalies occur as either isolated seismic features distributed along a discrete stratigraphic level, or are vertically stacked across multiple stratigraphic levels (Figs. 4, 7). Nearly all these seismic anomalies are related to the supra-volcanic faults (i.e. they are bound on one side by these faults; Figs. 4, 5f, 6).

Based on their seismic characteristics (e.g. enhanced, low-frequency and negative-polarity seismic reflections), we interpret these seismic anomalies as representing areas of free gas (e.g. Judd & Hovland, 2007; Cartwright et al., 2007). Strata beneath areas of stacked free gas layers are characterized by weak, low-frequency seismic reflections; this occurs due to absorption of the seismic signal by gas-charged layers (Fig. 4). So-called velocity 'push-downs' are indicative of low-acoustic velocities probably caused by free gas in the pore spaces (e.g. Judd & Hovland, 2007; Sun et al., 2012) (Fig. 4c).

Within borehole BY7-1, free gas is mainly found in siltstone and sandstone layers (Fig. 2). These gas-charged layers are usually characterized by anomalously low p-wave velocity (~0.3-0.8 km/s lower than the velocities of surrounding strata; Fig. 2), consistent with seismic evidence (i.e. push-downs) for slower velocities (Figs. 4a-c). Total gas is usually in excess of 30,000 ppm in gas-charged layers, which is higher than in those strata lacking gas (i.e. <10,000 ppm). $\delta^{13}C$ values gradually decrease upward from the top of the drilled volcano (-34‰ PDB) (Fig. 2). However, it is >-55‰ (PDB) even in the shallowest strata, indicating that the gas is mainly thermogenic (e.g. Tissot & Welte, 1984; Zhu et al., 2009).

Discussions

Interaction between volcano complexes and normal faults

The volcano intersected by the borehole BY7-1 formed in response to at least three eruptive episodes, separated by periods of deposition of limestone and claystone (Fig. 2). The occurrence of shallow-water limestone (Qin, 1996) between the eruptive products, as well as the petrologic characteristics of eruptive products (e.g. massive accumulation of volcanic-clastic deposits, glassy and welded textures; Ma et al., 2018), suggests volcanism occurred in a shallow, fully submarine setting (Zhao et al., 2016; Ma et al., 2018). Volcanism probably ceased around 17.5 Ma, given that the related volcanoes are draped by surface T5 (~17.5 Ma; Fig. 4). This interpretation is supported by the recovery of Early Miocene (17.1±2.5 Ma) igneous material from the crest of the volcano (Qin, 2000) (Fig. 2). Igneous rocks dominating the cores of the volcanoes have lower primary porosities and are thus less compactable than the surrounding clastic sediments (e.g. Chopra and Marfurt, 2012). We therefore interpret that the dome-shaped folds directly overlying the volcanoes formed due to differential compaction. Relatively slow and continuous growth of these folds is supported by the observations that related growth strata progressively thin towards to the fold and do not onlap a discrete surface (Figs. 4a, 7).

The faults located within sub-volcanic strata (i.e. below surface T5) correspond to those documented by Deng et al. (2018) in the adjacent Baiyun Sag (Fig. 1a), implying many may have been active before and during volcanism (i.e. during the Oligocene to Middle Miocene; ~32-16.5 Ma). The observation that volcanoes overlie faults, which occasionally terminate at volcano bases, and are typically elongated parallel to fault-strike (Figs. 3, 5a-b, 5d, 7, 9a), suggest the faults may have facilitated magma ascent. Such fault-controlled magma ascent is consistent with the spatial and genetically relationships between volcanoes and faults in active and ancient sedimentary basins (e.g. Gaffney et al., 2007; Mazzarini, 2007; Magee et al., 2013b, 2016; Isola et al., 2014; Weinstein et al., 2017), and in numerical models (e.g. Le Corvec et al., 2013; Maccaferri et al., 2014). Volcano growth by fault-controlled magma ascent is further supported by the across-fault thickening of volcanic strata; this indicates faulting and extrusion were synchronous (red dashed ellipses in Figs. 8a-b). We highlight that sub-vertical dykes, not hosted by faults, may have also fed the volcanoes. Dykes commonly intrude the crust during the continent rifting (e.g. Kendall et al., 2005; Maccaferri et al., 2014), but such structures are not typically imaged in seismic reflection data because their (sub-) vertical attitude does not reflect acoustic energy back to the surface (e.g. Phillips et al., 2017). Furthermore, even if present, dykes would likely be located in the very poorly imaged zone directly beneath the volcanoes, compromising their imaging and recognition (Figs. 4a-b, 7).

Supra-volcanic faults developed between surfaces T4 (16.5 Ma) and T1 (5.0 Ma), which bound Middle-Late Miocene strata, are younger than the early Middle Miocene (~>17.5 Ma) volcanoes. Some faults offsetting T0 (~2.58 Ma) indicate that they were also active in the Quaternary (Fig. 4). Because the supra-volcanic faults are: (i) clustered above the volcanoes (Figs. 4, 5b-d); (ii) terminate down-dip at the tops of volcanoes (e.g. Fig. 4a); and (iii) have similar strikes (~WNW) to the volcano long-axes (Figs. 5b-d, 9b-c), we suggest the volcanoes influenced their distribution and formation. We also note that dense zones of supra-volcano faults occur within and offset folded strata directly above the volcanoes. We consider two potential mechanisms that may have driven supra-volcanic faulting. First, volcanoes and their underlying intrusions can locally perturb a regional stress field associated with stretching of the crust. These perturbations influence the style and patterns of strain (e.g. Maccaferri et al., 2014; Magee et al., 2014; Lee et al., 2016; Weinstein et al., 2017). It is plausible the WNW-trending supra-volcanic faults formed to accommodate westward movement of the Philippine Plate, which commenced in the Middle Miocene (surface T3; ~13.8 Ma) (Lüdmann & Wong, 1999; Sun et al., 2014a), with strain being localized above the rigid volcanoes. An alternative interpretation is that the faults formed to accommodate stratal (outer-arc extension) bending associated with differential compaction above the volcanoes. These two models for fault generation are not mutually exclusive.

Focused fluid flow promoted by buried volcanoes and neotectonics

Our observations from seismic reflection data (Figs. 4, 5f, 6), combined with borehole and geochemical data (Fig. 2), show that free gas is locally preserved in clastic layers located directly above the volcanoes (Fig. 10). Areas of free gas are delineated by (Figs. 4, 5f, 6-7) or occur immediately above the tips of normal faults (Figs. 4c-d). These observations suggest the free gas likely migrated upward along these faults and charged the more porous sandstone and siltstone layers (Figs. 2, 10d). Whilst deep-seated faults could have provide long-lived pathways for fluid and gas (e.g. CO_2) ascent from mantle to the shallow free gas accumulations (e.g. Lee et al., 2016), chemical data show the free gas has a thermogenic origin (Fig. 2). This indicates the gas was sourced from thermally activated decomposition of relatively deeply buried (>900 m) organic material (e.g. remains of plant and animals). The thin, coarse-grained sediments (Eocene – Early Miocene) that directly underlie the volcanoes (Fig. 2) mean that the source rocks are lack and the thermogenic free gas cannot be generated in the study area (Yunkai Low Massif, Fig. 1a). Considering that the Baiyun Sag, which is located close to the study area (Fig. 1), is a hydrocarbon-rich 'kitchen' area with a sedimentary thickness of >10 km (e.g. Pang et al., 2008), it is likely that thermogenic hydrocarbons were sourced from there (Fig. 10d). Hydrocarbons may have migrated from the deep-seated source rock in the Baiyun Sag to structural highs in the Yunkai Low Massif (study area) through permeable strata and/or unconformities located along the western flank of the Baiyun Sag (Figs. 1a, 10d). Because they are mounded and represent natural four-way dip-closures, volcanoes in the Yunkai Low Massif may have temporarily housed gas. This interpretation is supported by the presence of dead oil within at least one of the volcanoes (Fig. 2). Gas may have also accumulated within the porous, folded layers/structural traps above the volcanoes (Fig. 2). The latter interpretation is confirmed by the presence of residual gas in supra-volcanic layers, with this gas expressed by relatively low p-wave velocities (~0.3-0.8 km/s lower than the velocities of surrounding strata) and high total gas readings (>30,000 ppm) (Fig. 2). The widespread, thick, very fine-grained sediments overlying the volcanoes likely serve as regional seals across the northern SCS (e.g. Zhao et al., 2009). Post-eruption faulting reduced the bulk permeability of the seal, permitting hydrocarbon migration along faults to shallower structural levels (Fig. 4). It is, however, difficult to precisely constrain when hydrocarbon leakage from the volcanoes occurred. Considering the Dongsha Event started at around ~10.5 Ma (peaking at ~5.3 Ma; Lüdmann & Wong, 1999; Zhao et al., 2012), and that this event triggered the hydrocarbon migration in the neighboring Baiyun Sag (e.g. Zhu et al., 2009, 2012), gas leakage in this study was also likely punctuated. The latest period of gas migration along the faults probably occurred in the Quaternary, based on the observations that the shallowest free gas occurs within uppermost Pliocene strata (Fig. 4b) and that many faults penetrate upward into Quaternary strata (Fig. 4).

Model for volcano-tectono interactions and related fluid flow

Here we propose a four-stage model to account for the link between magmatism, faulting and fluid flow in the northern SCS. In the first stage, crystalline basement of Yunkai Low Massif, which lay west of the Baiyun Sag, was deformed by deep-seated faulting (Fig. 10a). Magma was extruded onto the paleo-seabed in relatively shallow water (Qin, 1996; Yan et al., 2006). Magma likely ascended along the deep-seated faults (Figs. 8c-d, 10a). Though one sample from the erupted materials was dated to 35.5±2.78 Ma (Paleocene; Qin, 2000), how long magmatism lasted cannot be determined in this stage, because the base of the volcanic pile is not penetrated or dated.

During the second stage, coarse-grained clastic material was deposited, with intermittent periods of relatively weak volcanism; we infer punctuated volcanism based on the interbedding of sandstone and thin layers of volcanic eruptive material such as basalt and tuff (Figs. 2, 10b). Normal faulting, which occurred prior to the main Miocene eruptive phase, offset the clastic strata (Deng et al., 2018). Some of these faults linked with deep-seated, basement-involved faults (Figs. 7, 10b). After this relatively quiescent second stage, a second main period of intense volcanic activity, which was focused in this study, occurred. Several volcanic complexes were emplaced on the shallow paleo-seabed (Fig. 10c); volcanoes emplaced in this third stage were probably also fed by magma ascending along the deep-seated faults (Fig. 7). Volcanism ceased in the study area before ~17.5 Ma.

During the fourth and final stage (~17.5 Ma onwards), thick sequences of predominantly very fine-grained clastic material were deposited above the volcanoes (Fig. 10d). Another important period of normal faulting occurred during this stage, forming the supra-volcanic normal faults (Fig. 10d). Hydrocarbons sourced from the Baiyun Sag were transported along the flanks of Baiyun Sag through porous layers or along unconformities (Fig. 10d) (e.g. Pang et al., 2008; Zhu et al., 2009). These hydrocarbons probably temporarily accumulated within the topographic highs defined by the volcanoes, before migrating further upwards via the supra-volcanic normal faults (Figs. 4, 7-8, 10d).

Implication for hydrocarbon exploration and production

Drilling data indicates the volcanoes studied here lack live oil (Fig. 2). However, the presence of dead oil and minor staining suggests hydrocarbons migrated into and through the volcanoes. Regardless of whether the volcanoes served as reservoirs or simply as pathways for hydrocarbons, they clearly focused post-eruption fluid and gas flow (Fig. 4). Dome-shaped differential compaction folds above the volcanoes may have acted as structural traps for fluids and gases migrating upwards from the volcanoes or from the porous sediments lining unconformities developed on their flanks (Fig. 10d). However, faults within the folded strata allowed gas to leak upwards to shallower levels (Figs. 4, 10d). Our results suggest buried volcano-related, focused fluid and gas flow conduits could be a common occurrence in volcanogenic basins, particularly since differential compaction-related domes and related structures (e.g. normal faults) are often observed above many ancient, seismically imaged volcanoes (e.g. Li et al., 2015; Yang et al., 2016; Schofield et al., 2017). The presence, evolution and importance of these coupled systems will likely become clearer as more 2D and 3D seismic reflection data are available within volcanically influenced basins. The risk of seal degradation, and secondary migration and accumulation of hydrocarbons related to buried volcanoes should be taken into consideration during hydrocarbon exploration in such basins.

The accumulation of gas in shallowly buried and thus weakly lithified strata may have caused an increase pore pressure within those units. Overpressure of the gas-charged strata could represent a drilling hazard, with higher-than-expected pore pressures being encountered during drilling. Failure to accurate prognose such high pore pressures in such strata could lead to collapse of the wellbore and may even trigger a blow-out (e.g. Eruteya et al., 2015). Overpressure could also cause decrease the shear strength of particular units or interfaces, priming them (and the overlying material) to catastrophically fail and generate a submarine landslide in response to an appropriate trigger (e.g. seismicity, gas hydrate dissociation; e.g. Kvalstad et al., 2005). Such a scenario is envisaged in the nearby Baiyun Sag (Baiyun Slide; Sun et al., 2018). Because landslides can trigger tsunami and may damage seabed infrastructure, attention should be paid to the way in which deeply buried, non-inactive volcanoes influence subsurface flow of fluids and gases.

Conclusions

We used high-resolution 3D seismic data and borehole data from the northern South China Sea to document the impact of faults on magma ascent and the spatial location of volcanic centers, and the role the latter has on fluid flow. Volcanism was multi-staged, ceasing before ~17.5 Ma (T5), with migration of hydrocarbons lasting until the Early Pleistocene (~2.58 Ma). Hydrocarbons migrated upwards along post-eruption faults, which are related to regional stress and the bending of strata caused by differential compaction. The transported hydrocarbon (mainly methane) finally charged porous layers (sandstone and siltstone) offset by the post-eruption faults. This study shows that the volcano-related deformations can influence the surrounding, regional stress fields and subsurface fluid flow. These processes likely increase the bulk permeability of otherwise sealing sequences, facilitating the cross-stratal migration of hydrocarbons from deep sources to shallower reservoirs. This study highlights the underappreciated role buried volcanoes may have on focused, subsurface fluid flow. Shallow fluid and gas can drive the development of overpressure; not only this can cause problems when drilling wellbores, but it can prime material to catastrophically fail, which itself can drive the generation of tsunami and damage costly seabed infrastructure. Considering that buried volcanoes are widespread in both the passive and active continental margin basins, more attention should be paid to their role in controlling subsurface fluid flow.

Acknowledgements

This work was supported by the National Key R&D Program of China (No. 2018YFC0310000) the National Scientific Foundation of China (Grant Nos. 91528301, 41676051 and 41372112), and the Fundamental Research Funds for the Central Universities-the China University of Geosciences (Wuhan) (No. CUG160604). We thank the China National Offshore Oil Company for permission to release the data. Editor Cynthia Ebinger and two reviewers, Ovie Emmanuel Eruteya and Zewei Yao are thanked for their invaluable comments and suggestions which greatly improve the manuscript.

References

Aarnes, I., Podladchikov, Y., & Svensen, H. (2012). Devolatilization-induced pressure build-up: implications for reaction front movement and breccia pipe formation. *Geofluids*, 12, 265-279. doi: 10.1111/j.1468-

8123.2012.00368.x.

Babiker, M., & Gudmundsson, A. (2004). The effects of dykes and faults on groundwater flow in an arid land: the Red Sea Hills, Sudan. *Journal of Hydrology*, 297, 256-273. doi: 10.1016/j.jhydrol.2004.04.018.

Berndt, C., Skogly, O.P., Planke, S., Eldholm, O., & Mjelde, R. (2000). High-velocity breakup-related sills in the Vøring Basin, off Norway. *Journal of Geophysical Research-Solid Earth*, 105, (B12). doi: 10.1029/2000JB900217.

Briais, A., Patriat, P., & Tapponnier, P. (1993). Updated interpretation of magnetic anomalies and seafloor spreading stages in the South China Sea: implications for the Tertiary tectonics of Southeast Asia. *Journal of Geophysical Research-Solid Earth*, 98, 6299-6328. doi: 10.1029/92JB02280.

Calvès, G., Schwab, A.M., Huuse, M., Clift, P.D., Gaina, G., Jolley, D., Tabrez, A.R., & Inam, A. (2011). Seismic volcanostratigraphy of the western Indian rifted margin: The pre-Deccan igneous province. *Journal of Geophysical Research-Solid Earth*, 116, B01101. doi: 10.1029/2010JB000862.

Cartwright, J., Huuse, M., & Aplin, A. (2007). Seal bypass systems. *AAPG Bulletin*, 91, 1141-1166. doi: 10.1306/04090705181.

Chopra, S., & Marfurt, K.J. (2005). Seismic attributes-A historical perspective. *Geophysics*, 70, 3SO. doi: 10.1190/1.2098670.

Chopra, S., & Marfurt, K.J. (2012). Seismic attribute expression of differential compaction. The Leading Edge, 31, 1418-1422. doi: 10.1190/tle31121418.1.

Deng, P., Mei, L.F., Liu, J., Zheng, J.Y., Liu, M.H., Cheng, Z.J., & Guo, F.T. (2018). Episodic normal faulting and magmatism during the syn-spreading stage of the Baiyun sag in Pearl River Mouth Basin: response to the multi-phase seafloor spreading of the South China Sea. *Marine Geophysical Research*, in press. doi, 10.1007/s11001-018-9352-9.

Eruteya, O.E., Waldmann, N., Schalev, D., Makovsky, Y., & Ben-Avraham, Z. (2015). Intra- to post- Messinian deep-water gas piping in the Levant Basin, SE Mediterranean. *Marine and Petroleum Geology*, 66, 246-261. doi: 10.1016/j.marpetgeo.2015.03.007.

Franke, D. (2013). Rifting, lithosphere breakup and volcanism: comparison of magma-poor and volcanic rifted margins. *Marine and Petroleum Geology*, 43, 63-87. doi: 10.1016/j.marpetgeo.2012.11.003.

Gaffney, E.S., Damjanac, B., & Valentine, G.A. (2007). Localization of volcanic activity: 2. Effects of pre-existing structure. *Earth and Planetary Science Letters*, 263, 323-338. doi: 10.1016/j.epsl.2007.09.002.

Gudmundsson, A., & Løtveit, I.F. (2012). Sills as fractured hydrocarbon reservoirs: Examples and models. *Geological Society London Special Publications*, 374, 251-271. doi: 10.1144/SP374.5.

Hasenclever, J., Knorr, G., Rupke, L.H., Kohler, P., Morgan, J., Garofalo, K., Barker, S., Lohmann, G., & Hall, I.R. (2017). Sea level fall during glaciation stabilized atmospheric CO_2 by enhanced volcanic degassing. *Nature Communications*, 8, 15867. doi: 10.1038/ncomms15867.

Holford, S.P., Schofield, N., MacDonald, J.D., Duddy, I.R., & Green, P.F. (2012). Seismic analysis of igneous systems in sedimentary basins and their impacts on hydrocarbon prospectivity: Examples from the southern Australian margin. *APPEA Journal*, 52, 229-252. doi: 0.1071/AJ11017.

Holford, S.P., Schofield, N., & Reynolds, P. (2017). Subsurface fluid flow focused by buried volcanoes in sedimentary basins: Evidence from 3D seismic data, Bass Basin, offshore southeastern Australia. *Interpretation*, 5, SK39-SK50. doi: 10.1190/INT-2016-0205.1.

Huang, B.J., Xiao, X.M., & Zhang, M.Q. (2003). Geochemistry, grouping and origins of crude oils in the Western Pearl River Mouth Basin, offshore South China Sea. *Organic Geochemistry*, 34, 993-1008. doi: 10.1016/S0146-6380(03)00035-4.

Infante-Paez,L., & Marfurt, K.J. (2017).Seismic expression and geomorphology of igneous bodies: A Taranaki Basin, New Zealand, case study. *Interpretation*, 5, SK121-SK140. doi: 10.1190/INT-2016-0244.1.

Isola, I., Mazzarini, F., Bonini, M., & Corti, G. (2014). Spatial variability of volcanic features in early-stage rift settings: the case of the Tanzania Divergence, East African rift system. *Terra Nova*, 26, 461-468. doi: 10.1111/ter.12121.

Iyer, K., Schmid, D.W., Planke,S., & Millett, J. (2017). Modelling hydrothermal venting in volcanic sedimentary basins: Impact on hydrocarbon maturation and paleoclimate. *Earth and Planetary Science Letters*, 467, 30-42. doi: 10.1016/j.epsl.2017.03.023.

Jackson C.A-L., Schofield, N., & Golenkov, B. (2013). Geometry and controls on the development of igneous sill-related forced folds: A 2-D seismic reflection case study from offshore southern Australia. *Geological Society of America Bulletin*, 125, 1874-1890. doi: 10.1130/B30833.1.

Jamtveit, B., Svensen, H., Podladchikov, Y.Y., & Planke, S. (2004). Hydrothermal vent complexes associated with sill intrusions in sedimentary basins. In: Breitkreuz, C., Petford, N. (Eds.), Physical Geology of High-Level Magmatic Systems. Geological Society Publishing House, Bath, pp. 233-241.

Judd, A.G., & Hovland, M. (2007). Seabed Fluid Flow: The Impact on Geology, Biology and the Marine Environment. Cambridge University Press, Cambridge, pp. 163-178.

Kendall, J.M., Stuart, G.W., Ebinger, C.J., Bastow, I.D., & Keir, D. (2005). Magma-assisted rifting in Ethiopia. *Nature*, 433, 146.doi: 10.1038/nature03161.

Kvalstad, T.J., Andresen, L., Forsberg, C.F., Berg, K., Bryn, P., & Wangen, M. (2005). The Storegga slide: evaluation of triggering sources and slide mechanics. *Marine and Petroleum Geology*, 22, 245-256. doi: 10.1016/j.marpetgeo.2004.10.019.

Le Corvec, N., Spörli, K.B., Rowland, J., & Lindsay, J. (2013). Spatial distribution and alignments of volcanic centers: Clues to the formation of monogenetic volcanic fields. *Earth-Science Reviews*, 124, 96-114. doi: 10.1016/j.earscirev.2013.05.005.

Lee, H., Muirhead, J.D., Fischer, T.P., Ebinger, C.J., Kattenhorn, S.A., Sharp, Z.D., & Kianji, G. (2016). Massive and prolonged deep carbon emissions associated with continental rifting. *Nature Geoscience*, 9, 145-150. doi: 10.1038/NGEO2622.

Lester, R., Van Avendonk, H.J.A., McIntosh, K., Lavier, L., Liu, C.-S., Wang, T.K., & Wu, F. (2014). Rifting and magmatism in the northeastern South China Sea from wide-angle tomography and seismic reflection imaging. *Journal of Geophysical Research: Solid Earth*, 119, 2305-2323. doi: 10.1002/2013JB010639.

Li, C.F., Xu, X., Lin, J., Sun, Z., Zhu, J., Yao, Y.J., Zhao, X.X., Liu, Q.S., Kulhanek, D.K., Wang, J., Song, T.R., Zhao, J.F., Qiu, N., Guan, Y.X., Zhou, Z.Y., Williams, T., Bao, R., Briais, A., Brwon E.A., Chen, Y.F., Clift, P.D., Colwell, F.S., Dadd, K.A., Ding, W.W., Almeida, I.H., Huang, X.L., Hyun, S.M., Jiang, T., Koppers, A.A.P., Li, Q.Y., Liu, C.L., Liu, Z.F., Nagai, R.H., Peleo-Alampay, A., Su, X., Tejada, M.L.G., Rrinh, H.S., Yeh, Y.C., Zhang, C.L., Zhang, F., & Zhang, G.L. (2014). Ages and magnetic structures of the South China Sea constrained by the deep tow magnetic surveys and IODP Expedition 349. *Geochemistry, Geophysics, Geosystems*, 15, 4958-4983. doi: 10.1002/2014GC005567.

Lüdmann, T., & Wong, H.K. (1999). Neotectonic regime at the passive continental margin of northern South China Sea. *Tectonophysics*, 311, 113-138. doi: 10.1016/S0040-1951(99)00155-9.

Ma, B.J., Wu, S.G., Betzler, C., Qin, Z.L., Mi, L.J., Gao, W., Bai, H.Q., Wu, F., & Dong, D.D. (2018). Geometry, internal architecture, and evolution of buried volcanic mounds in the northern South China Sea. *Marine and Petroleum Geology*, 97, 540-555. doi: 10.1016/j.marpetgeo.2018.07.029.

Maccaferri, F., Rivalta,E., Keir, D., & Acocella, V. (2014). Off-rift volcanism in rift zones determined by crustal unloading. *Nature Geoscience*, 7, 297-300. doi: 10.1038/NGEO2110.

Magee, C., McDermott, K.G., Stevenson, C.T. & Jackson, C.A.L. (2014). Influence of crystallised igneous intrusions on fault nucleation and reactivation during continental extension. *Journal of Structural Geology*, 62, 183-193.doi:

10.1016/j.jsg.2014.02.003.

Magee, C., Duffy, O.B., Purnell, K., Bell, R.E., Jackson, C.A.-L., & Reeve, M.T. (2016). Fault-controlled fluid flow inferred from hydrothermal vents imaged in 3D seismic reflection data, offshore NW Australia. *Basin Research*, 28, 299-318. doi: 10.1111/bre.12111.

Magee, C., Hunt-Stewart, E., & Jackson, C.A.-L. (2013a). Volcano growth mechanisms and the role of sub-volcanic intrusions: Insights from 2D seismic reflection data. *Earth and Planetary Science Letters*, 373, 41-53. doi: 10.1016/j.epsl.2013.04.041.

Magee, C., Jackson, C.A.-L., & Schofield, N. (2013b). The influence of normal fault geometry on igneous sill emplacement and morphology. *Geology*, 41, 407-410. doi: 10.1130/G33824.1.

Magee, C., Muirhead, D., Karvelas, A., Holford, S.P., Jackson, C.A.L., Bastow, I.D., Schofield, N., Stevenson, C.T.E., McLean, C., McCarthy, W., & Shtukert, O. (2016). Lateral magma flow in mafic sill complexes. *Geosphere*, 12, 809-841. doi: 10.1130/GES01256.1.

Mazzarini, F. (2007). Vent distribution and crustal thickness in stretched continental crust: the case of the Afar Depression (Ethiopia). *Geosphere*, 3, 152–162.doi: 10.1130/GES00070.1.

Millett, J.M., Wilkins, A.D., Campbell, E., Hole, M.J., Taylor, R.A., Healy, D., Jerram, D.A., Jolley, D.W., Planke, S., Archer, S.G., & Blischke, A. (2016). The geology of offshore drilling through basalt sequences: Understanding operational complications to improve efficiency: *Marine and Petroleum Geology*, 77, 1177-1192. doi: 10.1016/j.marpetgeo.2016.08.010.

Monreal, F.R., Villar, H.J., Baudino, R., Delpino, D., & Zencich, S. (2009). Modeling an atypical petroleum system: A case study of hydrocarbon generation, migration and accumulation related to igneous intrusions in the Neuquen Basin, Argentina. *Marine and Petroleum Geology*, 26, 590-605. doi: 10.1016/j.marpetgeo.2009.01.005.

Moussallam, Y., Tamburello, G., Peters, N., Apaza, F., Schipper, C.I., Curtis, A., Aiuppa, A., Masias, P., Boichu, M., Bauduin, S., Barnie, T., Bani, P., Giudice, G., & Moussallam, M. (2017). Volcanic gas emissions and degassing dynamics at Ubinas and Sabancaya volcanoes; implications for the volatile budget of the central volcanic zone. *Journal of Volcanology and Geothermal Research*, 343, 181-191. doi: 10.1016/j.jvolgeores.2017.06.027.

Pang, X., Chen, C., Peng, D., Zhu, M., Shu, Y., He, M., Shen, J., & Liu, B. (2007). Sequence stratigraphy of deep-water fan system of Pearl River, South China Sea. *Earth Science Frontier*, 14, 220-229 (in Chinese with English abstract).

Pang, X., Chen, C.M., Peng, D.J., Zhou, D., Shao, L., He, M., & Liu, B.J. (2008). Basic geology of Baiyun deep-water area in the northern South China Sea. *China Offshore Oil & Gas*, 20, 216-222 (in Chinese with English abstract).

Planke, S., Rasmussen, T., Rey, S.S., & Myklebust, R. (2005). Seismic characteristics and distribution of volcanic intrusions and hydrothermal vent complexes in the Vøing and Møre basins. In: Dorj A.G., Vining, B.A. (Eds.), Petroleum Geology: North-Western Europe and Global Perspectives? Proceedings of the 6th Petroleum Geology Conference. Geological Society, London.

Phillips, T.B., Magee, C., Jackson, C.A.L., & Bell, R.E. (2018). Determining the three-dimensional geometry of a dike swarm and its impact on later rift geometry using seismic reflection data. *Geology*, 46, 119-122. doi: 10.1130/G39672.1.

Qin, G.Q. (1996). Application of micropaleontology to the sequence stratigraphic studies of late Cenozoic in the Zhujiang River Mouth Basin. *Marine Geology & Quaternary Geology*, 16, 1-17 (in Chinese with English Abstract).

Qin, G.Q. (2000). Comments on "Discussion on the Upper-Lower Tertiary boundary in Well BY7-1" of the Pearl River Mouth Basin. Journal of Stratigraphy, 24, 387-393 (in Chinese with English Abstract).

Rateau, R., Schofield, N., & Smith, M. (2013). The potential role of igneous intrusions on hydrocarbon migration, West of Shetland. *Petroleum Geosciences*, 19, 259-272. doi: 10.1144/petgeo2012-035.

Reynolds, P., Planke, S., Millett, J.M., Jerram, D.A., Trulsvik, M., Schofield, N., & Myklebust, R. (2017). Hydrothermal vent complexes offshore Northeast Greenland: A potential role in driving the PETM. *Earth and Planetary Science Letters*, 467, 72-78. doi: 10.1016/j.epsl.2017.03.031.

Reynolds, P., Schofield, N., Brown, R.J., & Holford, S.P. (2018). The architecture of submarine monogenetic volcanoes - insights from 3D seismic data. *Basin Research*, 30, 437-451. doi: 10.1111/bre.12230.

Schofield, N., Holford, S., Millett, J., Brown, D., Jolley, D., Passey, S., Muirhead, D., Grove, C., Magee, C., Murray, J., Hole, M., Jackson, C., & Stevenson, C. (2017). Regional magma plumbing and emplacement mechanisms of the Faroe-Shetland Sill Complex: Implications for magma transport and petroleum systems within sedimentary basins. *Basin Research*, 29, 41-63. doi: 10.1111/bre.12164.

Schutter, S.R. (2003). Hydrocarbon occurrence and exploration in and around igneous rocks. *Geological Society London Special Publications*, 214, 7-33. doi: 10.1144/GSL.SP.2003.214.01.02.

Sibuet, J.C., Yeh, Y.C., & Lee, C.S. (2016). Geodynamics of the South China Sea. *Tectonophysics*, 692, 98-119. doi: 10.1016/j.tecto.2016.02.022.

Sibuet, J.C., Hsu, S.K., Le Pichon, X., Le Formal, J.P., Reed, D., Moore, G., & Liu, C.S. (2002). East Asia plate tectonics since 15 Ma: constraints from the Taiwan region. *Tectonophysics*, 344, 103-134. doi: 10.1016/S0040-1951(01)00202-5.

Sun, Z., Xu, Z., Sun, L., Pang, X., Yan, C., Li, Y., Zhao, Z., Wang, Z., & Zhang, C. (2014a). The mechanism of post-rift fault activities in Baiyun Sag, Pearl River Mouth Basin. *Journal of Asian Earth Sciences*, 89, 76-87. doi: 10.1016/j.jseaes.2014.02.018.

Sun, Q.L., Cartwright, J., Xie, X.N., Lu, X.Y., & Yuan, S.Q. (2018). Reconstruction of repeated Quaternary slope failures in the northern South China Sea. *Marine Geology*, 401, 17-35. doi: 10.1016/j.margeo.2018.04.009.

Sun, Q.L., Wu, S.G., Cartwright, J., & Dong, D.D. (2012). Shallow gas and focused fluid flow systems in the Pearl River Mouth basin, northern South China Sea. *Marine Geology*, 315, 1-14. doi : 10.1016/j.margeo.2012.05.003.

Sun, Q.L., Wu, S.G., Cartwright, J., Wang, S.H., Lu, Y.T., Chen, D.X., & Dong, D.D. (2014b). Neogene igneous intrusions in the northern South China Sea: evidence from high resolution three dimensional seismic data. *Marine and Petroleum Geology*, 54, 83-95. doi: 10.1016/j.marpetgeo.2014.02.014.

Svensen, H., Planke, S., Jamtveit, B., & Pedersen, T. (2003). Seep carbonate formation controlled by hydrothermal vent complexes: A case study from the Vøing Basin, the Norwegian Sea. *Geo-Marine Letters*, 23, 351-358. doi: 10.1007/s00367-003-0141-2.

Svensen, H., Planke, S., Malthe-Sorenssen, A., Jamtveit, B., Myklebust, R., Rasmussen Eidem, T., & Rey, S.S. (2004). Release of methane from a volcanic basin as a mechanism for initial Eocene global warming. *Nature*, 429, 542-545. doi:

Svensen, H., Corfu, F., Polteau, S., Hammer, O., & Planke, S. (2012). Rapid magma emplacement in the Karoo Large Igneous Province. *Earth Planetary Science Letters*, 325, 1-9. doi: 10.1038/nature02566.

Tissot, B.P., & Welte, D.H. (1984). Petroleum Formation and Occurrence. Springer, Berlin, pp. 74-266.

Weinstein, A., Oliva, S.J., Ebinger, C.J., Roecker, S., Tiberi, C., Aman, M., Lambert, C., Witkin, E., Albaric, J., Gautier, S., Peyrat, S., Muirhead, J.D., Muzuka, A.N.N., Mulibo, G., Kianji, G., Ferdinand-Wambura, R., Msabi, M., Rodzianko, A., Hadfield, R., Illsley-Kemp, F., & Fischer, T.F. (2017). Fault-magma interactions during early continental rifting: Seismicity of the Magadi-Natron-Manyara basins, Africa. *Geochemistry, Geophysics, Geosystems*, 18, 3662-3686. doi:10.1002/2017GC007027.

White, N., Thompson, M., & Barwise, T. (2003). Understanding the thermal evolution of deep-water continental margins. *Nature*, 426, 334-343. doi: 10.1038/nature02133.

Wohletz, k., & Heiken, G. (1992). Volcanology and Geothermal Energy. University of California Press, pp. 415.

Yan, P., Deng, H., Liu, H., Zhang, Z., & Jiang, Y. (2006). The temporal and spatial distribution of volcanism in the South China Sea region. *Journal of Asian Earth Science*, 27, 647-659. doi: 10.1016/j.jseaes.2005.06.005.

Yang, J.F., Zhu, W.B., Guan, D., Zhu, B.B., Yuan, L.S., Xiang, X.M., Su, J.B., He, J.W., & Wu, X.H. (2016). 3D seismic interpretation of subsurface eruptive centers in a Permian large igneous province, Tazhong Uplift, central Tarim Basin, NW China. *International Journal of Earth Sciences*, 105, 2311-2326. doi: 10.1007/s00531-015-1289-5.

Yu, H.S. (1994). Structure, stratigraphy and basin subsidence of Tertiary basins along the Chinese southeastern continental margin. *Tectonophysics*, 253, 63-76. doi: 10.1016/0040-1951(94)90017-5.

Zhang, Q.X., & Huang, B.J. (1991). Genetic types and generation history of natural gases from major basins in the South China Sea. *China Offshore Oil & Gas*, 4, 5-13 (in Chinese with English Abstract).

Zhao, F., Alves, T.M., Wu, S.G., Li, W., Huuse, M., Mi, L.J., Sun, Q.L., & Ma, B.J. (2016). Prolonged post-rift magmatism on highly extended crust of divergent continental margins (Baiyun Sag, South China Sea). *Earth and Planetary Science Letters*, 445, 79-91. doi: 10.1016/j.epsl.2016.04.001.

Zhao, F., Wu, S.G., Sun, Q.L., Huuse, M., Li, W., & Wang, Z.J. (2014). Submarine volcanic mounds in the Pearl River Mouth Basin, northern South China Sea. *Marine Geology*, 355, 162-172. doi: 10.1016/j.margeo.2014.05.018.

Zhao, M., He, E., Sibuet, J.-C., Sun, L., Qiu, X., Tan, P., & Wang, J. (2018). Postseafloor spreading volcanism in the central east South China Sea and its formation through an extremely thin oceanic crust. *Geochemistry, Geophysics, Geosystems*, 19, 621-641. doi: 10.1002/2017GC007034.

Zhao, S.J., Wu, S.G., Shi, H.S., Dong, D.D., & Chen, D.X. (2012). Structures and dynamic mechanism related to the dongsha movement at the northern margin of South China Sea. *Progress in Geophysics*, 27, 1008-1019 (in Chinese with English abstract).

Zhu, W., Huang, B., Mi, L., Wilkins, R.W.T., Fu, N., & Xiao, X. (2009). Geochemistry, origin, and deep-water exploration potential of natural gases in the Pearl River Mouth and Qiongdongnan Basins, South China Sea. *AAPG Bulletin*, 93, 741-761. doi: 10.1306/02170908099.

Zhu, W.L., Zhong, K., Li, Y.C.,Xu, Q., & Fang, D.Y. (2012). Characteristics of hydrocarbon accumulation and exploration potential of the northern South China Sea Dee pwater Basins. *Chinese Science Bulletin*, 57, 1833-1841. doi: 10.1007/s11434-011-4940-y.

Zou, H., Li, P., & Rao, C. (1995). Geochemistry of Cenozoic volcanic rocks in Zhu Jiangkou basin and its geodynamic significance. *Geochimica*, 24, 33-45.

Figure Captions

Figure 1: (a) Geological setting and subdivision of the Pearl River Mouth Basin (enlargement of pink square in the top left corner). The study area (blue square: 3D seismic survey) is located in the Yunkai Low Massif between the Kaiping Sag and the Baiyun Sag. Well location (BY7-1) is marked with green star. The boundary faults are modified from Pang et al. (2007) and Sun et al. (2014a). Top left: Geological background of the South China Sea; (b) Schematic stratigraphic column of the Pear River Mouth Basin (modified from Pang et al. (2008) and Sun et al. (2014b)). SR = seismic reflectors, TE= tectonic evolution, BE = basin evolution, DE= sedimentary environment; (c) Geoseismic interpretation of the study area; see (a) for location.

Figure 2: Correlation of seismic profile and borehole (BY7-1). Five layers of free gases (mainly shown as enhanced negative seismic anomalies or blanking reflection with low frequency) are drilled by BY7-1, which can also be identified in the well loggings and geochemical analysis. The items marked with ® and © (Lithology, K-Ar dating, Ages and depositional environments (DEs), $\delta^{13}C$ (planktonic foraminifera) and $\delta^{18}O$ (planktonic foraminifera)) are modified from Qin. (1996) and Qin. (2000). Parts of the well loggings are also used in Qin. (1996), Qin. (2000) and Zhao et al. (2016). The item ($\delta^{13}C$) marked with§ is from the analysis of headspace gas.

Figure 3: Three-dimensional visualization of the top of volcano complexes (Surface T5). The volcano complexes show as positive reliefs. Normal faults which present as linear structures with sharp boundaries are also observed.

Figure 4: (a)-(d): Seismic characteristics of free gas, normal faults and volcano complexes. See locations of (a)-(c) in Fig. 6c and location of (d) in Fig. 5a. Free gas shows as stacked or isolated enhanced seismic anomalies with low frequencies. It distributes in several layers and its extent is outlined by normal faults. Sometimes, wipe-out zone (blanking seismic reflections) and pull-down seismic reflections are observed underneath the enhanced seismic anomalies. Faults are denser within the strata above volcano complexes (light green polygon). Some large normal faults can penetrate into the basement and they extend upward to surface T0. The semi-transparent green and blue squares are the windows of RMS amplitudes of Fig. 6a and Fig. 6b, respectively. Variance slice locations of Fig. 5c (straight dashed blue line) and Fig. 5d (straight dashed red line) are also labeled. TV = Top of volcano; BV = Base of volcano; PDs = Pull-down seismic reflections.

Figure 5: The configurations of volcano complexes, free gas and normal faults. (a) Top of volcano complexes (Surface T5). The volcano complexes show as positive reliefs; (b) Thickness of the volcano complexes, which shows that the volcano complexes linearly trend NW-SE; (c) and (d) variance slices of 1150 ms and 1800 ms (in the post-eruption strata). Faults can be clearly observed; (e) variance slice of 30 ms below the base of volcano complexes (in the pre-eruption strata) and faults are also clearly identified; (f) RMS amplitude (1150 ms with windows of ±25 ms) of the entire 3D survey. The free gas has very high RMS amplitude and it only distributes in the southeastern part of the 3D seismic survey.

Figure 6: Enlargements showing the relationships of volcano complexes, free gas and normal faults.

(a) and (b): RMS amplitude of 1150 ms with windows of ±50 ms and 1800 ms with windows of ±100 ms. Free gas shows as high values of RMS amplitude (warm colors). See locations in Fig. 5; (c) and (d): outlines of volcano complexes and interpreted faults are superimposed on the RMS amplitude maps. Free gas is usually limited by faults and locates within the extents of volcano complexes; (e) and (f): line drawings of (c) and (d). The superimposed relationships of volcano complexes, normal faults and free gas are clearly shown.

Figure 7: (a) and (b) uninterpreted and interpreted profiles show seismic characteristics of the strata above the volcano complex. See location in Fig. 5a. These strata are bended and normal faults densely occurred within these strata. Free gas is closely linked to the normal faults and the seismic reflections below free gas are blanking or wipe-out. The semi-transparent green and blue squares are the windows of RMS amplitudes of Fig. 6a and Fig. 6b, respectively. Variance slice locations of Fig. 5c (straight dashed blue line) and Fig. 5d (straight dashed red line) are also labeled.

Figure 8: (a) Normal faults crosscut the volcano complex and (b) its line drawing. The eruptive materials in the hanging wall are thicker than its footwall counterpart. See location in Fig. 6c; (c) Normal faults immediately terminated at the base of volcano complexes and (d) its line drawing. See location in Fig. 5a.

Figure 9: (a)-(c): Fault strikes of Figure 5e (n = 202), 5c (n = 90) and 5d (n = 196). Both the faults within the pre-eruption and post-eruption strata have similar strikes (NWW-SEE); (d)-(f): Fault lengths of Figure 5e, 5c and 5d. The faults have small scales and usually below 3 km long; (h)-(j):

Fault strike vs fault length of Figure 5e, 5c and 5d.

Figure 10: Model for the magmation, faulting and focused fluid flow in the study area. (a) Fault fed pioneer magma extruded in the shallow water at a very early stage; (b) In the quiescent stage, detrital sediments deposited on the pioneer eruptive materials; (c) Large-scale magma extruded onto the paleo-seabed and formed the mounded volcano complexes; (d) Thermogenic hydrocarbon accumulated to the volcano complexes or the traps above it. Faulting directly occurred within the strata above volcano complex and hydrocarbon leakage through these faults.

Figure 1

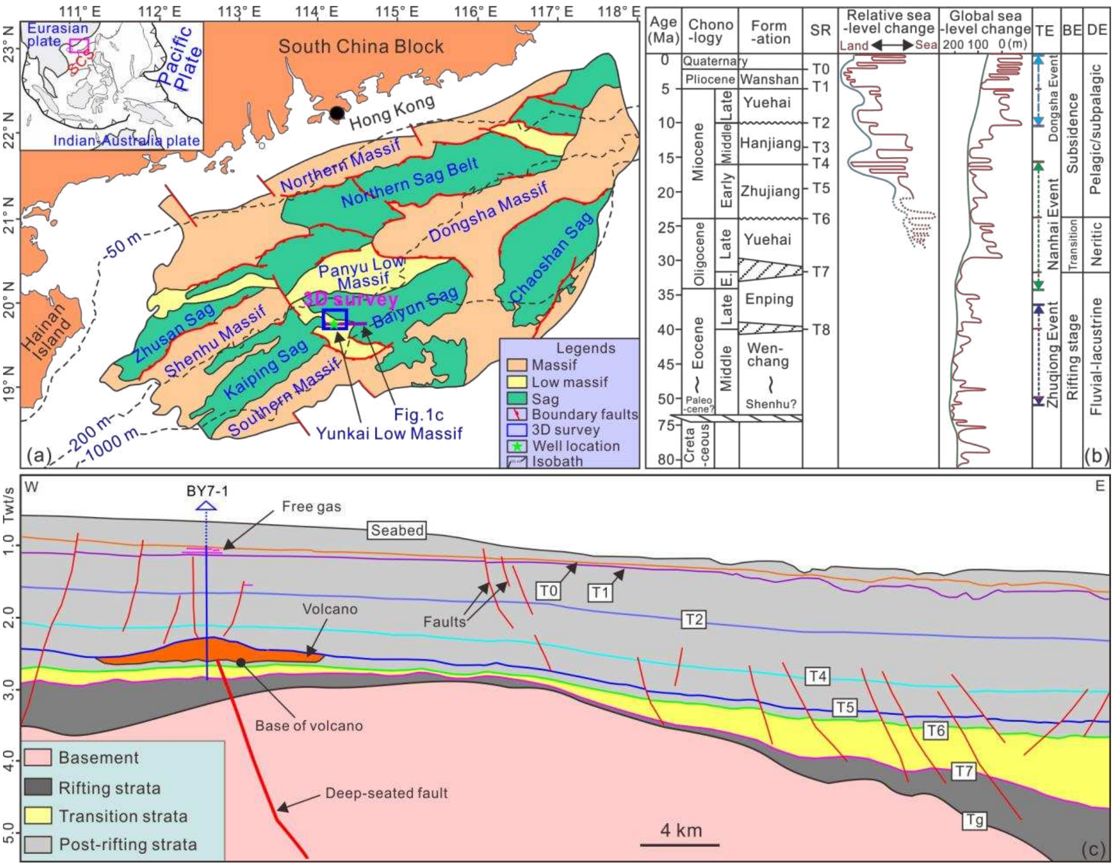

Figure 1: (a) Geological setting and subdivision of the Pearl River Mouth Basin (enlargement of pink square in the top left corner). The study area (blue square: 3D seismic survey) is located in the Yunkai Low Massif between the Kaiping Sag and the Baiyun Sag. Well location (PY7-1) is marked with green star. The boundary faults are modified from Pang et al. (2007) and Sun et al. (2014a). Top left: Geological backgrounds of the South China Sea. (b) Schematic stratigraphic column of the Pear River Mouth Basin (modified from Pang et al. (2008) and Sun et al. (2014b)). SR = seismic reflectors, TE= tectonic evolution, BE = basin evolution, DE= sedimentary environment. (c) Geoseismic interpretation of the study area; see (a) for location.

Figure 2

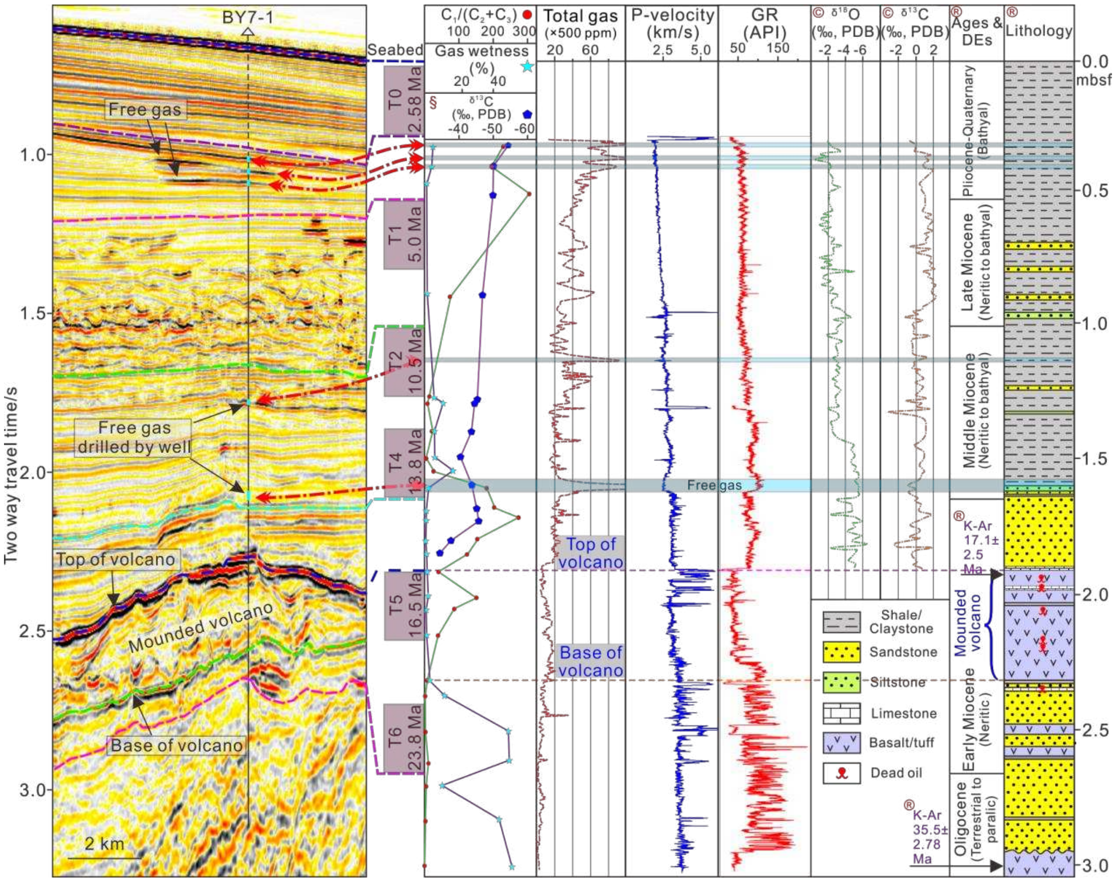

Figure 2: Correlation of seismic profile and borehole (BY7-1). Five layers of free gases (mainly shown as enhanced negative seismic anomalies or blanking reflection with low frequency) are drilled by BY7-1, which can also be identified in the well loggings and geochemical analysis. The items marked with ® and © (Lithology, K-Ar dating, Ages and depositional environments (DEs), $\delta^{13}C$ (planktonic foraminifera) and $\delta^{18}O$ (planktonic foraminifera)) are modified from Qin. (1996) and Qin. (2000). Parts of the well loggings are also used in Qin. (1996), Qin. (2000) and Zhao et al. (2016). The item ($\delta^{13}C$) marked with§ is from the analysis of headspace gas.

Figure 3

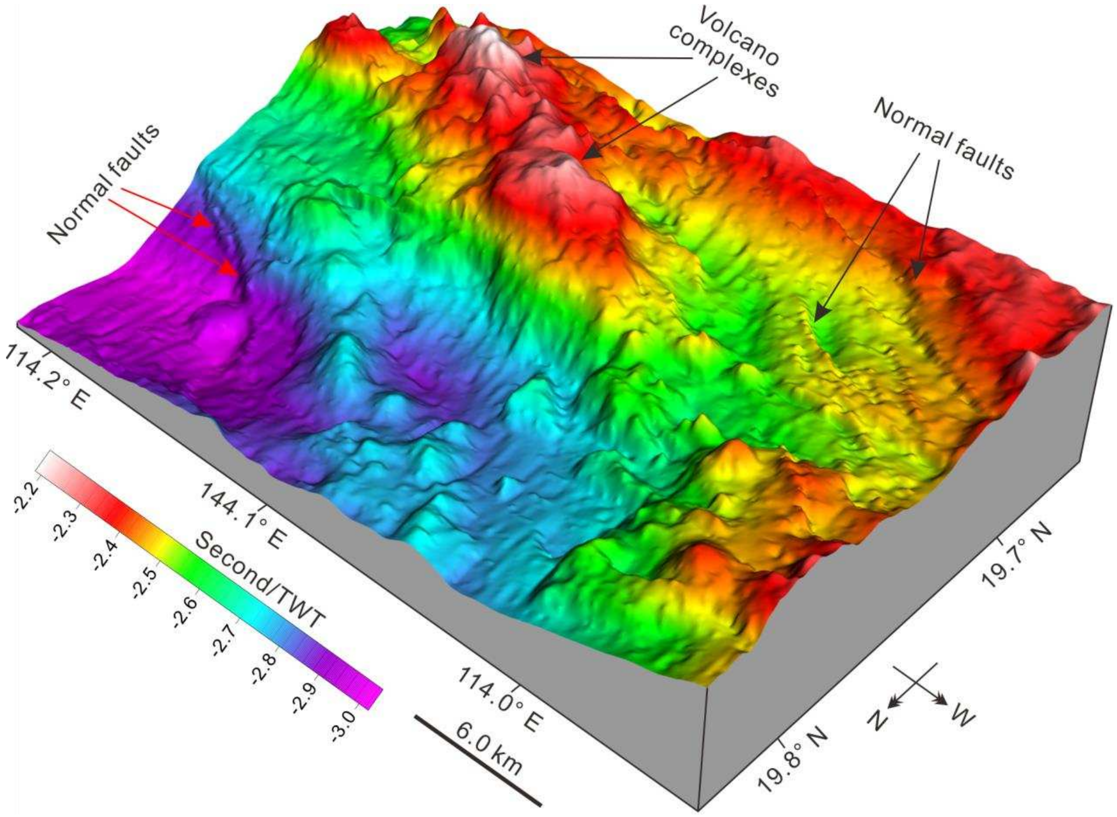

Figure 3: Three-dimensional visualization of the top of volcano complexes (Surface T5). The volcano complexes show as positive reliefs. Normal faults which present as linear structures with sharp boundaries are also observed.

Figure 4

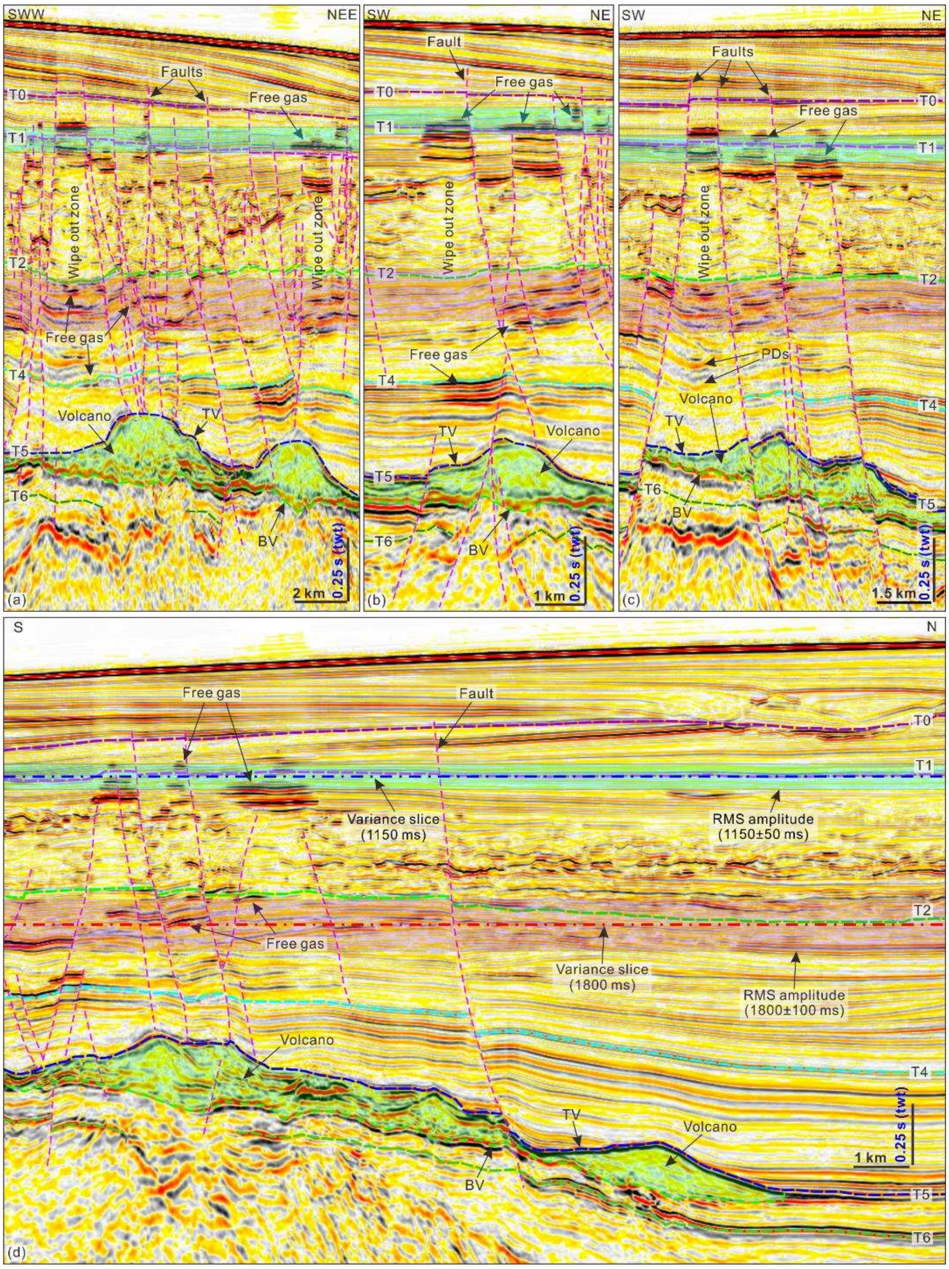

Figure 4: (a)-(d): Seismic characteristics of free gas, normal faults and volcano complexes. See locations of (a)-(c) in Fig. 5i and location of (d) in Fig. 5a. Free gas shows as stacked or isolated enhanced seismic anomalies with low frequencies. It distributes in several layers and its extent is outlined by normal faults. Sometimes, wipe-out zone (blanking seismic reflections) and pull-down seismic reflections are observed underneath the enhanced seismic anomalies. Faults are denser within the strata above volcano complexes (light green polygon). Some large normal faults can penetrate into the basement and they extend upward to surface T0. The semi-transparent green and blue squares are the windows of RMS amplitudes of Fig. 6a and Fig. 6b, respectively. Variance slice locations of Fig. 5c (straight dashed blue line) and Fig. 5d (straight dashed red line) are also labeled. TV = Top of volcano; BV = Base of volcano.

Figure 5

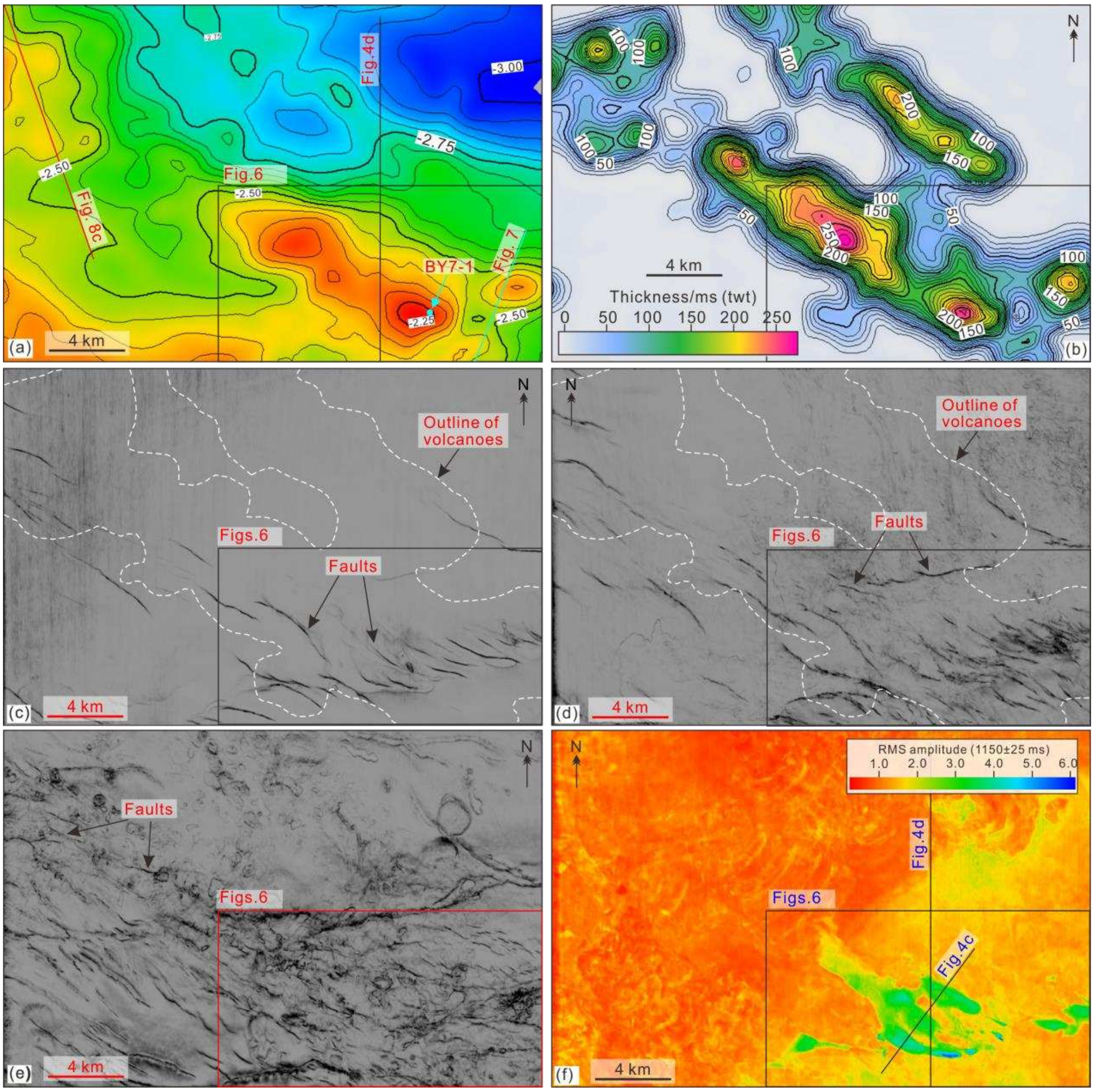

Figure 5: The configurations of volcano complexes, free gas and normal faults. (a) Top of volcano complexes (Surface T5). The volcano complexes show as positive reliefs; (b) Thickness of the volcano complexes, which shows that the volcano complexes linearly trend NW-SE; (c) and (d) variance slices of 1150 ms and 1800 ms (in the post-eruption strata). Faults can be clearly observed; (e) variance slice of 30 ms below the base of volcano complexes (in the pre-eruption strata) and faults are also clearly identified; (f) RMS amplitude (1150 ms with windows of ±25 ms) of the entire 3D survey. The free gas has very high RMS amplitude and it only distributes in the southeastern part of the 3D seismic survey.

Figure 6

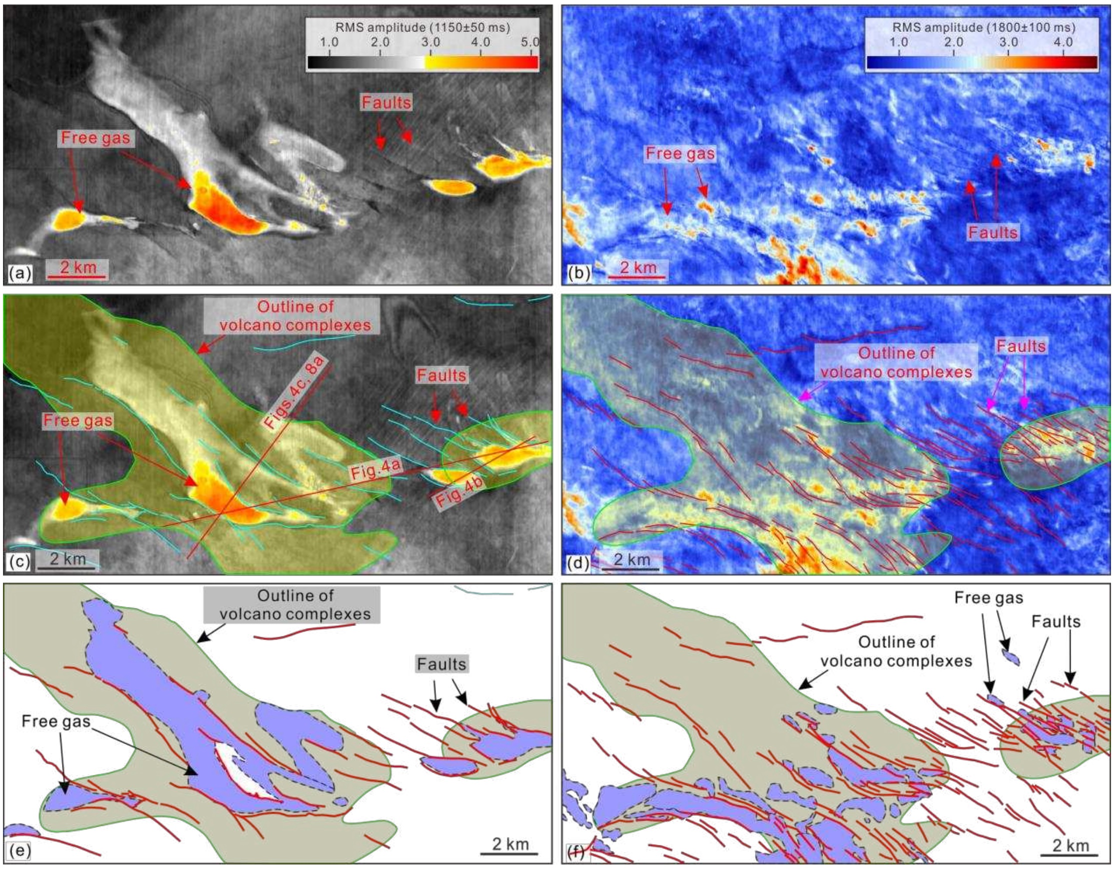

Figure 6: Enlargements showing the relationships of volcano complexes, free gas and normal faults. (a) and (b): RMS amplitude of 1150 ms with windows of ±50 ms and 1800 ms with windows of ±100 ms. Free gas shows as high values of RMS amplitude (warm colors). See locations in Fig. 5; (c) and (d): outlines of volcano complexes and interpreted faults are superimposed on the RMS amplitude maps. Free gas is usually limited by faults and locates within the extents of volcano complexes; (e) and (f): line drawings of (c) and (d). The superimposed relationships of volcano complexes, normal faults and free gas are clearly shown.

Figure 7

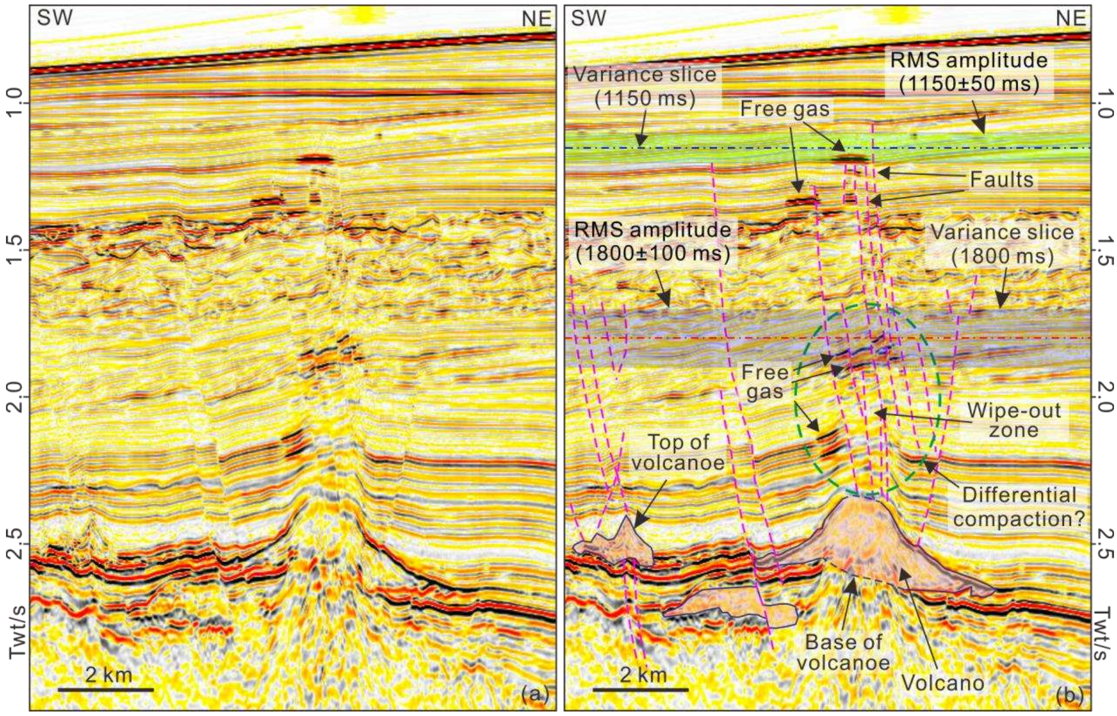

Figure 7: (a) and (b) uninterpreted and interpreted profiles show seismic characteristics of the strata above the volcano complex. See location in Fig. 5a. These strata are bended and normal faults densely occurred within these strata. Free gas is closely linked to the normal faults and the seismic reflections below free gas are blanking or wipe-out. The semi-transparent green and blue squares are the windows of RMS amplitudes of Fig. 6a and Fig. 6b, respectively. Variance slice locations of Fig. 5c (straight dashed blue line) and Fig. 5d (straight dashed red line) are also labeled.

Figure 8

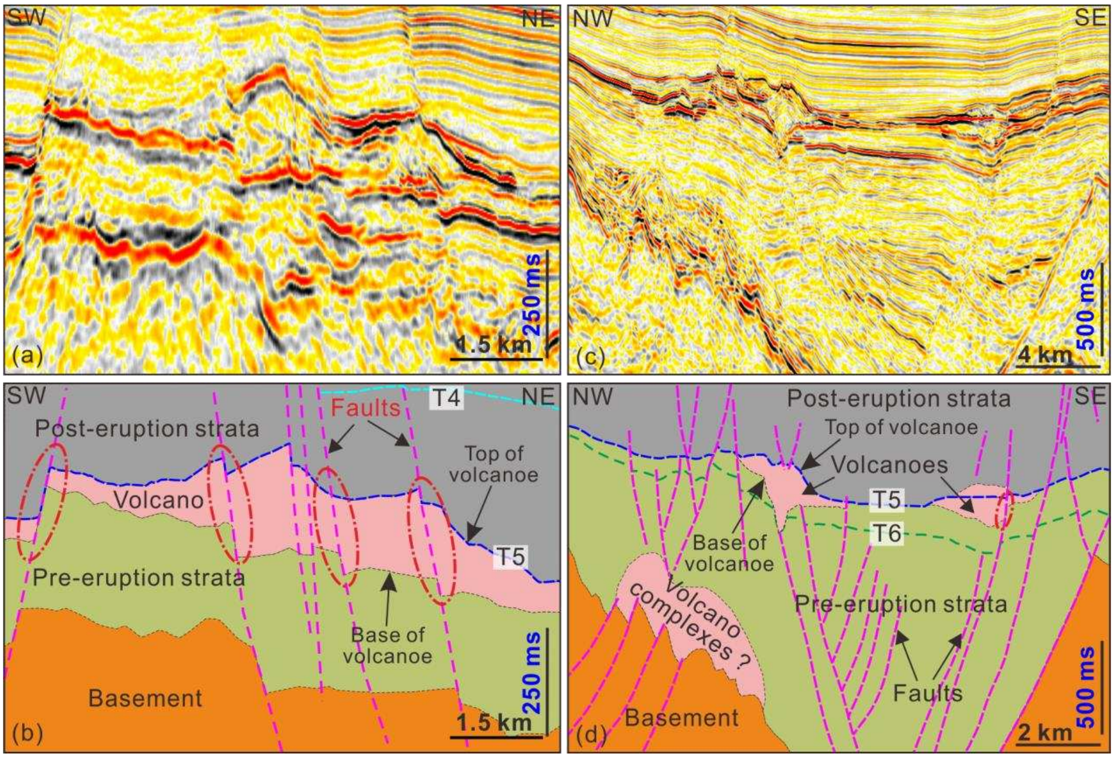

Figure 8: (a) Normal faults crosscut the volcano complex and (b) Its line drawing. The eruptive materials in the hanging wall are thicker than its footwall counterpart. See location in Fig. 6c; (c) Normal faults immediately terminated at the base of volcano complexes and (d) Its line drawing. See location in Fig. 5a.

Figure 9

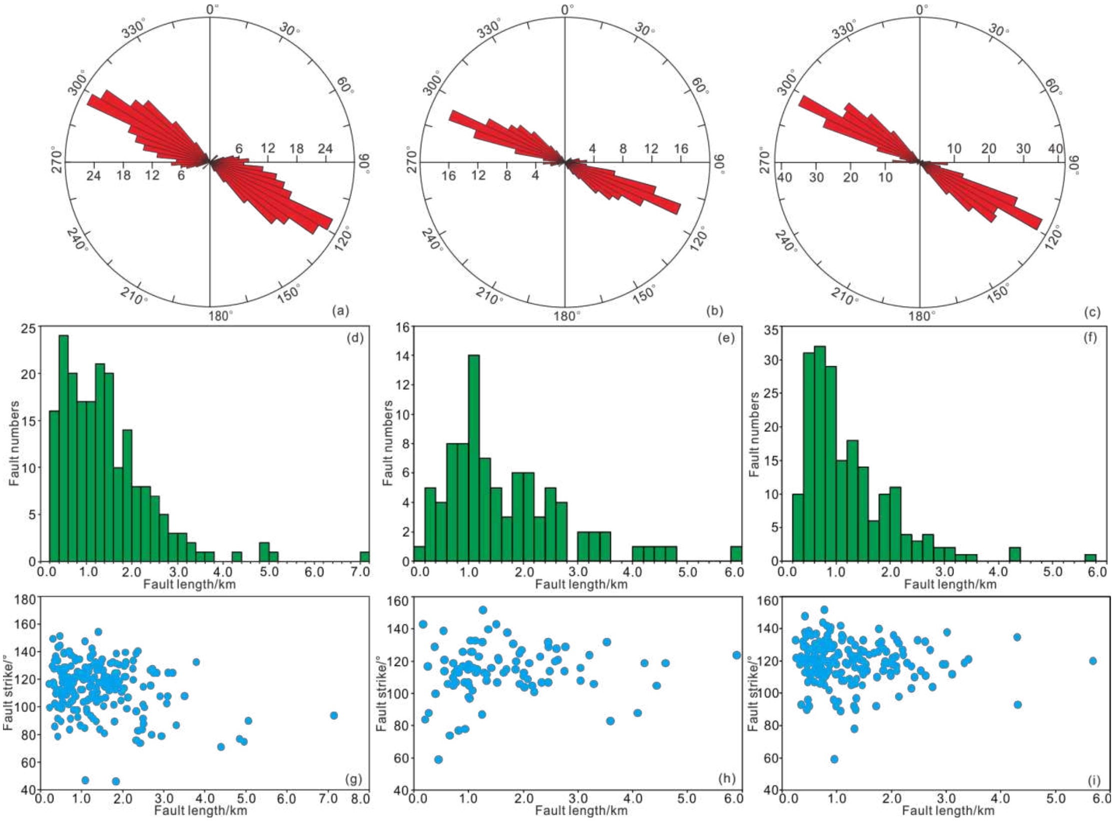

Figure 9: (a)-(c): Fault strikes of Figure 5e (n = 202), 5c (n = 90) and 5d (n = 196). Both the faults within the pre-eruption and post-eruption strata have similar strikes (NWW-SEE); (d)-(f): Fault lengths of Figure 5e, 5c and 5d. The faults have small scales and usually below 3 km long; (h)-(j): Fault strike vs fault length of Figure 5e, 5c and 5d.

Figure 10

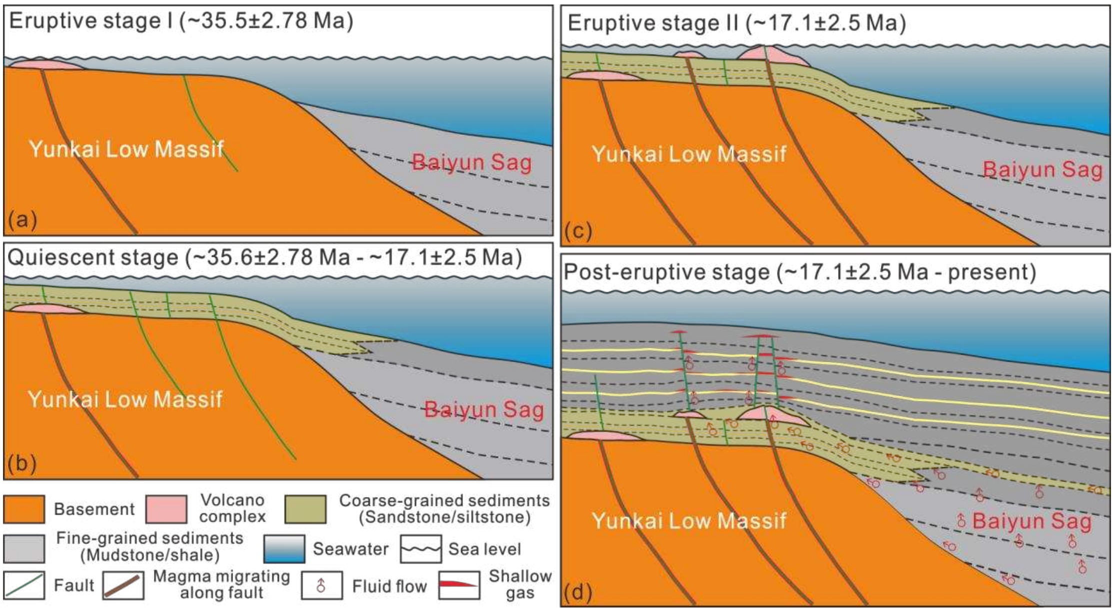

Figure 10: Model for the magmation, faulting and focused fluid flow in the study area. (a) Fault fed pioneer magma extruded in the shallow water at a very early stage; (b) In the quiescent stage, detrital sediments deposited on the pioneer eruptive materials; (c) Large-scale magma extruded onto the paleo-seabed and formed the mounded volcano complexes; (d) Thermogenic hydrocarbon accumulated to the volcano complexes or the traps above it. Faulting directly occurred within the strata above volcano complex and hydrocarbon leakage through these faults.